CARBON 86 (2015) 310–317

Available at www.sciencedirect.com

ScienceDirect

journal homepage: www.elsevier.com/locate/carbon

Graphene/acid assisted facile synthesis of structure-tuned Fe_3O_4 and graphene composites as anode materials for lithium ion batteries

Yucheng Dong [a,b], Kam Chuen Yung [b,*], Ruguang Ma [c], Xia Yang [a], Ying-San Chui [a], Jong-Min Lee [c], Juan Antonio Zapien [a,*]

[a] Center of Super-Diamond and Advanced Films (COSDAF), City University of Hong Kong, Hong Kong
[b] Department of Industrial and Systems Engineering, The Hong Kong Polytechnic University, Hong Kong
[c] School of Chemical & Biomedical Engineering, Nanyang Technological University, 62 Nanyang Drive, Singapore 637459, Singapore

ARTICLE INFO

Article history:
Received 19 August 2014
Accepted 30 January 2015
Available online 7 February 2015

ABSTRACT

Structure-tuned Fe_3O_4 and graphene composites were prepared using a facile graphene/acid assisted facile one-pot hydrothermal method. The structural characteristics of Fe_3O_4 can be tuned by adjusting the initial molar ratio between iron acetylacetonate and citric acid. The citric acid serves dual function as a reducing agent during the production of Fe_3O_4 nanoparticles (NPs), and as a bridging agent which under optimized conditions can result in mesoporous Fe_3O_4 nanospheres (NSs) self-assembled by numerous Fe_3O_4 NPs. The fabricated mesoporous Fe_3O_4 NSs and graphene composites were evaluated as potential anode materials for lithium ion batteries. These composites exhibit better electrochemical performance with high reversible capacity, good rate capability and cyclic stability derived from their unique mesoporous structural features.

1. Introduction

In the past decade, lithium ion batteries (LIBs) have become the predominant power source for portable electronic devices and electric vehicles due to their high energy density and long cycle life [1,2]. While graphite is the most successful anode material for LIBs, inherent limitations arise because of its low theoretical capacity (372 mAh g^{-1}) [3]. As a result, unprecedented global research interest is underway to develop high performance electrode materials for LIBs in order to satisfy the ever-increasing market demands [4,5]. Transition metal oxides with high theoretical capacity (~500–1000 mAh g^{-1}) have been extensively investigated as alternative anode materials for high performance LIBs [6–9]. Among them, Fe_3O_4 is the most attractive candidate to substitute conventional graphite because of its high theoretical capacity (924 mAh g^{-1}), environmental benignity, cost-efficient, and natural abundance. However, use of Fe_3O_4 presents added complications due to suffers from poor cycling stability caused by drastic volume variation and severe particles aggregation during reversible conversion reaction between Li^+ ions and Fe_3O_4 which results in electrode partial pulverization and integrity loss over several discharge/charge cycles. Furthermore, the high intrinsic resistance of Fe_3O_4 and poor charge transfer and ionic diffusion lead to additional performance degradation [10]. According to previous reports, the widely used approach to circumvent these issues is to combine nanosized structures of designed morphology with carbon-

* Corresponding authors.
E-mail addresses: Wincokc.yung@polyu.edu.hk (K.C. Yung), apjazs@cityu.edu.hk (J.A. Zapien).
http://dx.doi.org/10.1016/j.carbon.2015.01.062
0008-6223/

based conducting matrixes to form hybrid composites resulting in the potential multiple advantages including: shortened Li^+ ions diffusion path lengths; enlarged contact area between electrode and electrolyte; improved electronic conductivity; and alleviated mechanical stress during Li^+ ion insertion/extraction [11–15].

Graphene is one of the most promising of such carbon-based conducting matrixes; this is because of its unique properties, such as ultra-thin structure, high specific area, excellent electrical conductivity, and mechanical flexibility [16,17]. Therefore, graphene-based metal oxide composites have been widely used as electrode materials for LIBs, the improved electrochemical performance originates from synergetic effects between graphene and active materials: graphene sheets serve not only as structural buffer against structural deformation but also as a conductive network thus facilitating electrical conductivity [18–24]. However, the morphological effect of metal oxides fabricated via the same method on their electrochemical performance in these composites has been seldomly investigated.

In this report we investigate the morphology effect of electrode materials prepared using a graphene/acid assisted facile one-pot hydrothermal route to prepare Fe_3O_4 and graphene composites. Using iron acetylacetonate, citric acid, and graphene oxide (GO) as source materials, we show that the structure of Fe_3O_4 can be tuned by adjusting the initial molar ratio between iron acetylacetonate and citric acid. When the initial molar ratio is 3:2, the Fe^{3+} ions were *in situ* reduced to Fe^{2+} and further formed Fe_3O_4 NPs (~8–20 nm) anchored on graphene sheets. However, when the initial molar ratio changes to 3:3, the numerous Fe_3O_4 NPs (~15 nm) self-assemble into mesoporous Fe_3O_4 NSs (~100 nm) with unconspicuous interior hollow spaces decorated on graphene. The self-assembled mesoporous Fe_3O_4 NSs and graphene (Fe_3O_4-NS/G) composites exhibit improved electrochemical performance due to their unique and synergetic structural features.

2. Experiment

2.1. Preparation of Fe_3O_4-NP/G and Fe_3O_4-NS/G composites

GO was prepared from natural graphite powder using a modified Hummers' method (see ESI for details) [25]. The Fe_3O_4-NP/G and Fe_3O_4-NS/G composites were prepared via a simple hydrothermal method. In the typical synthesis of Fe_3O_4-NP/G composites, 40 mg GO was dissolved in 40 mL deionized water by mild sonication for 1 h. Next, 2 mmol citric acid was added and dissolved. Then, 3 mmol iron (III) acetylacetonate ($Fe(acac)_3$; 97%, Aldrich) was added to the resulting solution and stirred at 80 °C for 2 h to form a crimson solution. The resultant solution was transferred to a Teflon-lined stainless steel autoclave (50 mL in volume) and heated at 200 °C for 12 h before cooling down to room temperature. The obtained product was centrifuged and washed several times with alcohol and deionized water before drying at 60 °C for 10 h; the powder thus obtained was further annealed at 500 °C for 3 h in a tube furnace under nitrogen atmosphere to obtain well-crystallized Fe_3O_4-NP/G composites. The Fe_3O_4-NS/G composites were synthesized and treated under the same experimental conditions, except that the citric acid in the precursor solution was increased to 3 mmol. For comparison, pure Fe_3O_4 NPs were prepared using the same experimental procedures as Fe_3O_4-NS/G composites but without graphene. In addition, the comparative graphene electrode was prepared through reduced GO by hydrazine hydrate.

2.2. Characterization

The crystallographic characteristics of the products were studied by X-ray diffraction (XRD, Philips PW 1830); which also enabled particle size estimation using the Scherrer equation, $L = K\lambda/\beta\cos\theta$, where K is the Scherrer constant (0.89), λ is the X-ray wavelength, β is the line broadening at half the maximum intensity (FWHM), θ is the Bragg diffraction angle. Raman spectroscopy (Renishaw in via 2000, 600 nm excitation laser) was employed to verify chemical bonding characteristics of graphene. Specific surface area was estimated from nitrogen adsorption–desorption isotherms at 77 K using a NOVA 1200e Surface Area & Pore Size Analyzer (Quantachrome Instruments). Prior to absorption experiments, the samples were degassed at 150 °C for 2 h. Thermogravimetric analysis (TGA, Q50) was performed to evaluate the content of graphene under air atmosphere with a heating rate of 10 °C min^{-1}. The morphological characteristics were investigated by scanning electron microscopy (SEM; Philips, XL 30FEG), transmission electron microscopy (TEM; Philips, CM20), and high-resolution TEM (HRTEM; CM200 FEG).

The working electrodes were prepared by mixing 80 wt% active material, 10 wt% acetylene carbon black, and 10 wt% polyvinylidene fluoride (PVDF) binder dissolved in 1-methyl-2-pyrrolidinone (NMP) solvent to form a slurry. After coating the slurry on copper foil, the electrode was dried at 100 °C for 10 h in vacuum to remove the solvent. Electrochemical measurements were carried out using coin-type cells (2032) assembled in an argon-filled glovebox with lithium metal foil (Aldrich, USA) as counter/reference electrode, Celgard 2032 (Celgard, Inc., USA) serves as the separator and $LiPF_6$ (1 mol/L) was dissolved in a mixture of ethylene carbonate/dimethyl carbonate (1:1 in volume) as the electrolyte. Cyclic voltammograms (CVs) measurements were performed using a CHI-660C electrochemical workstation at a scanning rate of 0.1 mV s^{-1} in a potential range from 5 mV to 3.0 V. Galvanostatic discharge/charge cycles were tested in the voltage range from 5 mV to 3.0 V using different constant current densities on an Arbin Instruments (BT 2000, College Station, Texas, USA) battery cycler at room temperature. Electrochemical impedance spectroscopy (EIS) was carried out on a ZAHNER-elektrik IM6 over a frequency range of 100 kHz to 5 mHz.

3. Results and discussion

The XRD patterns of as-synthesized Fe_3O_4-NP/G and Fe_3O_4-NS/G composites, Fig. 1a, show all the diffraction peaks and relative intensities are in good agreement with those of Fe_3O_4 (Magnetite, PDF, 00-001-1111). The strong diffraction peaks indicate good crystallinity of Fe_3O_4 phases with average particle size, calculated from the largest diffraction peak (3 1 1)

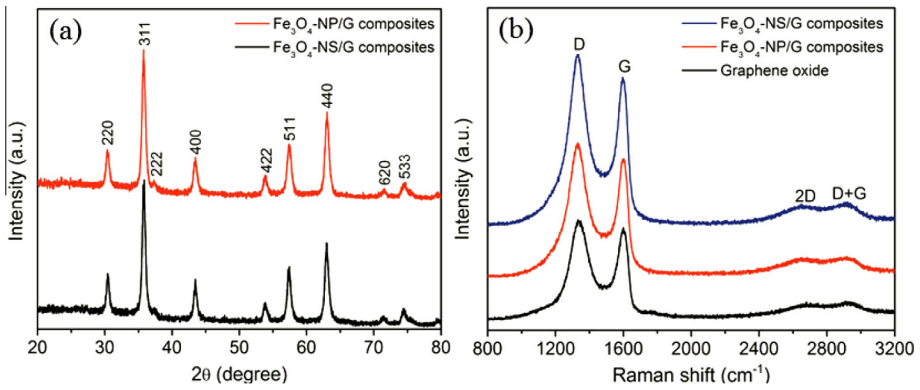

Fig. 1 – (a) XRD patterns of Fe_3O_4-NP/G and Fe_3O_4-NS/G composites; (b) Raman spectra of Fe_3O_4-NP/G composites, Fe_3O_4-NS/G composites, and GO. (A color version of this figure can be viewed online.)

through the Scherrer's formula, estimated to be ~13.8 and ~14.2 nm for Fe_3O_4-NP/G and Fe_3O_4-NS/G composites, respectively. However, no obvious diffraction peak of graphite was detected in the XRD patterns, indicating that the graphene sheets are not well crystallized. These results confirm that both Fe_3O_4-NP/G and Fe_3O_4-NS/G composites present the same crystallographic structure and similar crystalline size. The Fe_3O_4-NP/G and Fe_3O_4-NS/G composites were characterized by Raman spectroscopy to monitor the structural change of carbon network occurred during chemical processing from GO to graphene. Raman spectra of GO, Fe_3O_4-NP/G composites, and Fe_3O_4-NS/G composites are shown in Fig. 1b. The typical Raman spectrum of GO has two prominent peaks located at 1601 and 1348 cm^{-1} corresponding to the G and D bands, respectively. Two general characteristics of reduced GO is the shift to lower wavenumber of the G band, and the increase of peak intensity ratio between D and G bands (I_D/I_G) relative to a value of ~1.06 for GO. The Raman spectra of Fe_3O_4-NP/G and Fe_3O_4-NS/G composites show both G and D bands with the G band shifts to 1595 cm^{-1} while the I_D/I_G ratio for Fe_3O_4-NP/G and Fe_3O_4-NS/G composites are calculated to be ~1.12 and ~1.14, respectively, consistent with the reduction of GO during the hydrothermal reaction process. The presence of a peak at 2649 cm^{-1} according to the overtone of the D band and the peak at 2920 cm^{-1} can be ascribed to the (D + G) band which also shows a substantial increase in the disorder degree in graphene sheets [26].

The microstructure of as-synthesized Fe_3O_4-NP/G composites was characterized by SEM, TEM, and HRTEM, as shown in Fig. 2. It can be seen from Fig. 2a that small Fe_3O_4 NPs are closely anchored on the surface of graphene sheets. Fig. 2b presents TEM image of Fe_3O_4-NP/G composites. It can be observed that the two-dimensional thin graphene layers are decorated with Fe_3O_4 NPs with a size range of ~8–20 nm which is in accordance with XRD estimated crystalline size by Scherrer's equation. In addition, both the outline of graphene sheets and Fe_3O_4 NPs can be clearly observed, and there is no apparent aggregation of Fe_3O_4 NPs on the graphene layers. The HRTEM image of an individual Fe_3O_4 nanoparticle is shown in the inset of Fig. 2b which reveals the single-crystalline nature of Fe_3O_4 NPs. The morphology of Fe_3O_4 can be tuned by adjusting the initial molar ratio of iron acetylacetonate and citric acid. In particular, the self-assembled mesoporous Fe_3O_4 NSs and graphene composites can be obtained when 3 mmol citric acid is used keeping all experimental conditions identical. The SEM image in Fig. 2c shows the Fe_3O_4 NSs are well wrapped by graphene sheets. The TEM image in Fig. 2d further reveals that Fe_3O_4 NSs are well anchored on graphene layer with an average size of ~100 nm and a noticeable low density center. The high resolution TEM image of a single Fe_3O_4 nanosphere, inset of Fig. 2d, clearly shows the mesoporous structure of Fe_3O_4 NSs, with a clear interior hollow spaces, formed by the aggregation of many nano-sized Fe_3O_4 NPs (~15 nm) in agreement with the average particle size calculated from XRD results in Fig. 1a. The special structural features of void spaces among self-assembled NPs and interior hollow spaces are expected to accommodate large strain resulting from the Li^+ ions insertion/extraction as well as to provide short paths for Li^+ ions diffusion during the cycling process [27–29]. It should be noted that sonication was used during the TEM specimen preparation which demonstrates that there is a strong interaction between Fe_3O_4 NSs and graphene sheets rather than just simply mixing up or blending with each other. The HRTEM image (Fig. S1, see ESI for details) shows the characteristic lattice fringes of composed Fe_3O_4 NPs in Fe_3O_4-NS/G composites. The crystal lattice spacing is 0.252 nm which can be assigned to the (311) plane of cubic Fe_3O_4.

To illustrate the influence of citric acid content on the structural features of Fe_3O_4, a new product was fabricated using 4 mmol citric acid in the precursor solution but otherwise the same experimental procedures. The morphology of the resultant composites was determined by SEM analyses as shown in Fig. S2 (see ESI for details); in this case larger (~150–300 nm) and irregular Fe_3O_4 NSs wrapped by graphene sheets are obtained. These results are in support the interlinking role of citric acid in the formation of self-assembly of small Fe_3O_4 NPs into larger mesoporous Fe_3O_4 NSs. In this hydrothermal system, GO was found to play an important role in the formation of final products. No homogeneous NPs (Fig. S3, see ESI for details) or NSs (Fig. S4, see ESI for details) are generated in absence of GO. We speculated that the formation of product may be based on a heterogeneous nucleation process, in which the oxy-functional groups and defect sites on graphene sheets act as nucleation centers due to their high surface energy. These results demonstrated

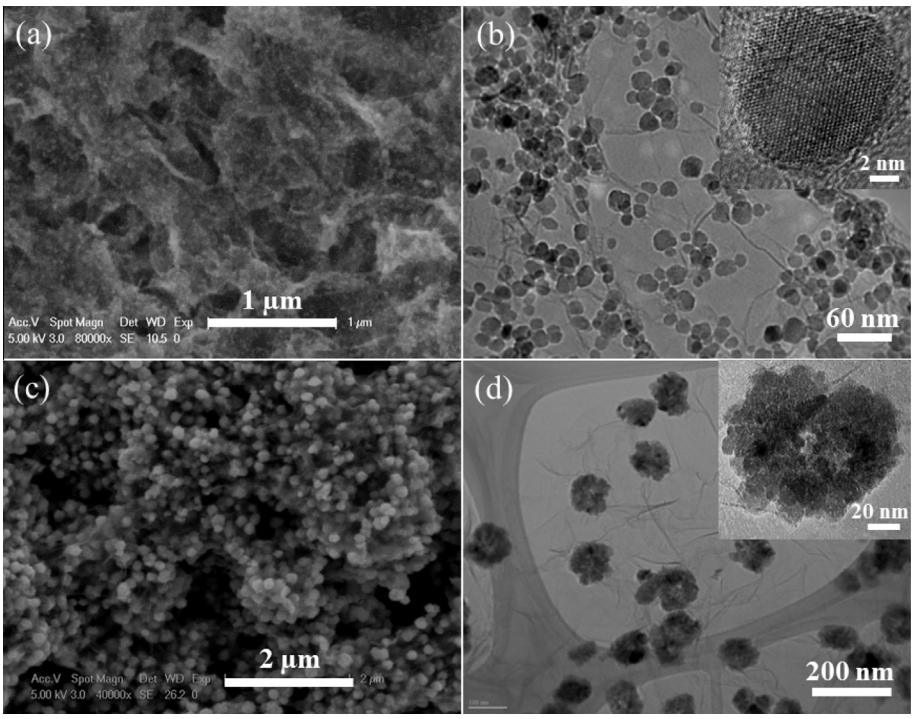

Fig. 2 – (a) SEM and (b) TEM images of Fe_3O_4-NP/G composites; and (c) SEM and (d) TEM images of Fe_3O_4-NS/G composites. The insets in (b) and (d) show the corresponding typical HRTEM images of the products.

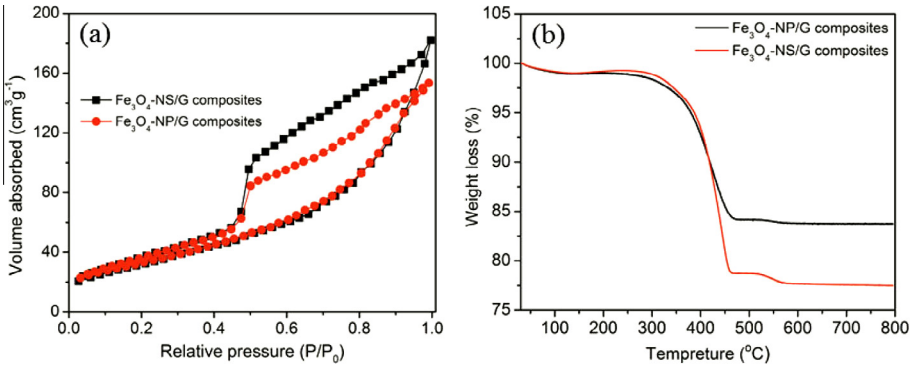

Fig. 3 – (a) Nitrogen adsorption/desorption isotherms, and (b) TGA spectra of Fe_3O_4-NP/G and Fe_3O_4-NS/G composites. (A color version of this figure can be viewed online.)

that graphene sheets help prevent Fe_3O_4 NPs from agglomeration and enable a good dispersion of Fe_3O_4 NPs or NSs over the graphene sheets.

To demonstrate the existence of void spaces between neighboring self-assembled NPs and interior hollow spaces, nitrogen adsorption/desorption isotherms were utilized to investigate the surface area of Fe_3O_4-NP/G and Fe_3O_4-NS/G composites. The isotherms in Fig. 3a can be categorized as type IV with hysteresis loop in the ~0.4–1.0 range of relative pressure according to the international union of pure and applied chemistry classification, confirming their mesoporous structure. The Brunauer–Emmett–Teller (BET) specific area of Fe_3O_4-NP/G and Fe_3O_4-NS/G composites are 120 and 121 $m^2 g^{-1}$, and the corresponding pore volumes are 0.247 and 0.319 $cm^3 g^{-1}$, respectively. The Barrett–Joyner–Halenda (BJH) pore sizes for Fe_3O_4-NP/G composites are randomly positioned in the regions of ~3–8 nm, in contrast to the Fe_3O_4-NS/G composites, the pore sizes are mainly distributed at ~4, ~6 and ~10 nm, as shown in Fig. S5 (see ESI for details). We speculate that the large pore volume of Fe_3O_4-NS/G composites caused by the presence of internal hollow spaces as observed in TEM images, and the void spaces among aggregated NPs. In order to quantify the weight percentage of Fe_3O_4 in these composites, TGA was carried out from room temperature to 800 °C under flowing air, so that Fe_3O_4 is oxidized to Fe_2O_3 and carbon is oxidized to CO_2, as shown in Fig. 3b. A theoretical weight increase of 3.45% is obtained because each Fe_3O_4 can combine 1/2 O unit [30]. The small weight loss below 150 °C is perhaps due to the evaporation of moisture or gaseous content in the composites [31]. From the remaining

weight of Fe_2O_3, the original weight fraction of Fe_3O_4 is calculated to be ~80.4% and ~74.3% for Fe_3O_4-NP/G and Fe_3O_4-NS/G composites, respectively.

The electrochemical performance of Fe_3O_4-NP/G and Fe_3O_4-NS/G composites were first investigated by CV at a scan rate of 0.1 mV s^{-1} within the voltage window of 0.005–3.0 V (*vs.* Li^+/Li) for the first five cycles, as shown in Fig. 4a and b, respectively. In the first cathodic scan, the strong and broad cathodic peaks at voltage potential of ~0.67 and ~0.61 V were observed for Fe_3O_4-NP/G and Fe_3O_4-NS/G composites, respectively, which attributed to the reduction of Fe^{3+} and Fe^{2+} to Fe^0, and the formation of a solid electrolyte interphase (SEI) layer [32]. Additional peaks located at 0.91 for Fe_3O_4-NP/G composites and at 1.52 V for Fe_3O_4-NS/G composites can be assigned to irreversible $Li_xFe_3O_4$ [33]. In the first anodic scan, two small peaks at 1.68 and 1.92 V for Fe_3O_4-NP/G composites, and at 1.64 and 1.87 V for Fe_3O_4-NC/G composites, were recorded due to the oxidation of Fe^0 to Fe^{3+} and Fe^{2+}. After the first cycle, both cathodic and anodic peaks shift to higher voltage and the corresponding current peaks decrease revealing the existence of certain degree of irreversibility of the redox reaction. While the CV changes continue in the Fe_3O_4-NP/G composites, changes of peak intensity and integrated areas for both cathodic and anodic peaks of Fe_3O_4-NS/G composites are very limited after the first cycle, suggesting that lithium ions insertion/extraction takes place to the same extent and demonstrating the superior reversibility of Fe_3O_4-NS/G composites.

The discharge/charge profiles of Fe_3O_4-NP/G and Fe_3O_4-NS/G composites are shown in Fig. 4c and d, respectively, between 5 mV and 3.0 V at a current density of 200 mA g^{-1}. The first discharge and charge capacity are ~1760 and ~1100 mAh g^{-1} for Fe_3O_4-NP/G composites, ~2060 and ~1240 mAh g^{-1} for Fe_3O_4-NS/G composites, respectively. The initial high discharge capacity has been widely observed for transition metal oxide anodes and is attributed to the formation of a SEI layer and the larger electrochemical active surface area of graphene and/or the grain boundary area of nano-sized Fe_3O_4 particles [34,35]. In fact, high experimental lithium storage capacity in these materials can also be attributed to these same reasons: first, the reversible electrolyte decomposition at low voltages results in extra lithium ion adsorption/desorption on the reversible SEI that results while cycling [10]; second, the reaction of oxygen-containing functional groups on graphene sheets with lithium ions can further contribute to the lithium storage capacity [36]. The irreversible capacity loss with respect to the first scan is thus attributed to the initial incomplete conversion reaction of the unstable SEI layer which is also consistent with the CV results in Fig. 4 showing additional peaks present only in the first cathodic scan [37,38]. After five discharge/charge cycles, the Fe_3O_4-NS/G composites exhibit a high discharge capacity of ~1030 mAh g^{-1}, and the corresponding Coulombic efficiency is 97.2%. In contrast, the discharge capacity of Fe_3O_4-NP/G composites drops to ~910 mAh g^{-1}, and the corresponding Coulombic efficiency is 89.2%.

The comparative cycling performance of Fe_3O_4-NS/G and Fe_3O_4-NP/G composites at a current rate of 0.2 C for 160 cycles (1 C = 1000 mA g^{-1}) is shown in Fig. 5a. For Fe_3O_4-NS/G composites, the reversible capacity remains stable at ~1025 mAh g^{-1} up to 50 cycles, and then slowly drops to ~920 mAh g^{-1} until ~100 cycles. After that it starts to increase

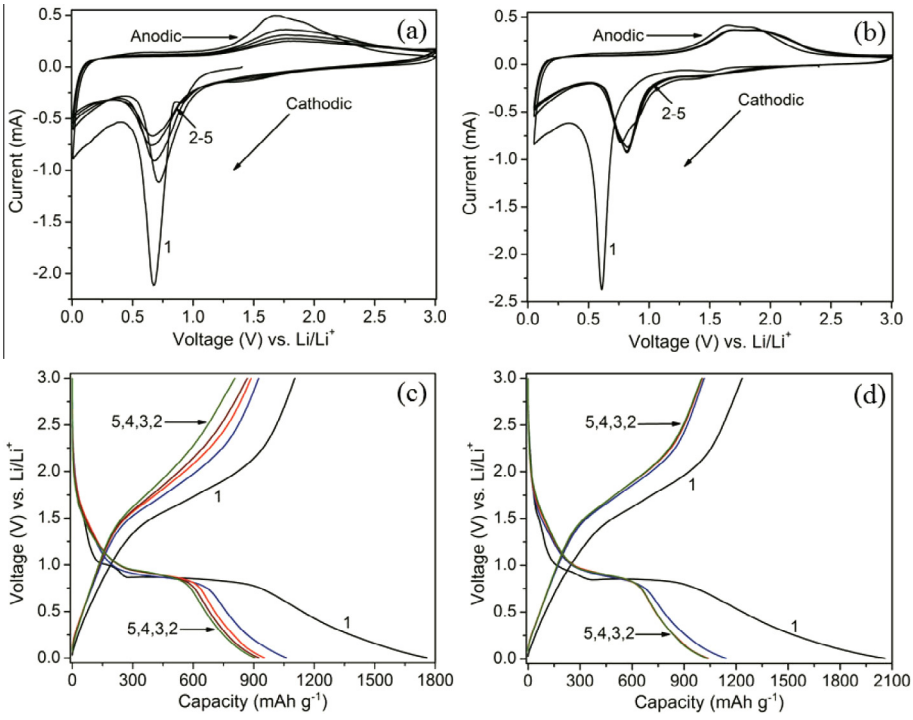

Fig. 4 – CV characteristics of (a) Fe_3O_4-NP/G composites and (b) Fe_3O_4-NS/G composites in a voltage range of 0.01–3.0 V at a scanning rate of 0.1 mV s^{-1}. Discharge/charge profiles of (c) Fe_3O_4-NP/G composites and (d) Fe_3O_4-NS/G composites between 5 mV and 3.0 V at a current density of 200 mA g^{-1}. (A color version of this figure can be viewed online.)

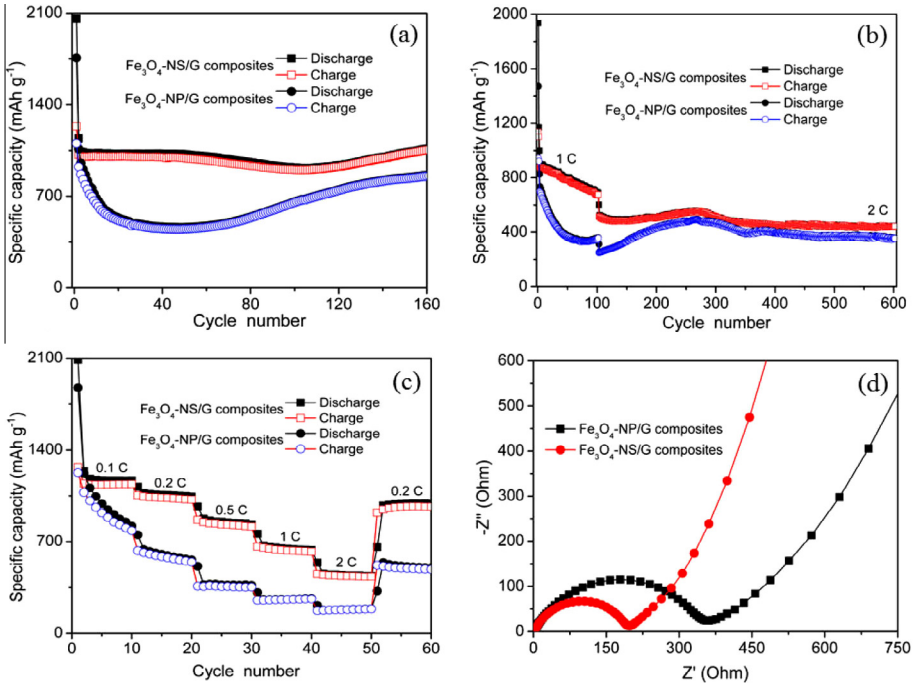

Fig. 5 – (a and b) Comparative cycling performance of Fe_3O_4-NS/G and Fe_3O_4-NP/G composites at different current densities. (c) Rate capability of Fe_3O_4-NS/G and Fe_3O_4-NP/G composites at various current densities. (d) Nyquist plots (Z' *vs.* $-Z''$) of Fe_3O_4-NS/G and Fe_3O_4-NP/G composites. (A color version of this figure can be viewed online.)

and reaches to ~1070 mAh g^{-1} after 160 cycles. In contrast, the reversible capacity of Fe_3O_4-NP/G composites fades rapidly to ~460 mAh g^{-1} after ~50 cycles and then gradually increases to ~860 mAh g^{-1} after 160 cycles. The capacity rise after prolonged cycling has been widely described for various nanostructured metal oxide electrodes and is attributed to the partial re-activation of irreversible Li_2O formed during the early cycles and resulting from the electrochemical grinding effect [39,40]. The better cyclic retention of Fe_3O_4-NS/G composites could originate from their unique structural features. During the cycling process, stable thin passivating SEI films would be formed outside the mesoporous Fe_3O_4 NSs due to the decomposition of electrolyte after the first few cycles, however, further formation is terminated due to the electronically insulating nature of the SEI film [41]. Moreover, the void spaces between the aggregated NPs and interior hollow spaces of mesoporous Fe_3O_4 nanospheres alleviate the volume variation resulting from the Li^+ ions insertion/extraction and provide short path for charge transfer and Li^+ ions diffusion during cycling process. Thus, the Fe_3O_4-NS/G composites present better cycling performance after the formation of stable SEI films. In contrast, the larger initial capacity drop for Fe_3O_4-NP/G composites is attributed to thicker SEI films formed over discharge/charge cycles. The large surface area of Fe_3O_4 NPs caused rupture of new formed SEI films due to the mechanical strain generated by the volume variation upon cycling, and then thick SEI films formed on the surface of Fe_3O_4 NPs, which degrades the electrochemical performance of the electrode [10,29]. As shown in Fig. 5a, this interpretation is consistent with the observed capacity loss of Fe_3O_4-NP/G composites that during the first 50 cycles, whereas the capacity loss for Fe_3O_4-NS/G composites quickly stop after the first several cycles. To evaluate the cyclic stability of the electrodes, new cells were assembled and tested at 1 C for 100 cycles, and then following at 2 C for 500 cycles, as shown in Fig. 5b. For Fe_3O_4-NS/G composites, the reversible capacity remains stable at ~445 mAh g^{-1} up to 600 cycles, in contrast to the Fe_3O_4-NS/G composites, the reversible capacity decreased to ~350 mAh g^{-1} after 600 cycles, which demonstrated the superior cycling performance of Fe_3O_4-NS/G composites. To clarify the synergistic effect between Fe_3O_4 and graphene for electrochemical performance enhancement, we also tested pure Fe_3O_4 NPs and graphene under the same electrochemical conditions. The results for Fe_3O_4 NPs and graphene show low capacities of ~290 and ~250 mAh g^{-1} after 160 cycles as shown in Fig. S6 (see ESI for details). The low capacity of pure Fe_3O_4 NPs has been recognized to the cyclically rupture and growth of SEI which cause high resistance to ion transport and electronic conductivity [10,29]. In contrast, the restacking of graphene sheets in the cycling process leads to low capacity of pure graphene anode [42]. For Fe_3O_4 and graphene composites, the restacking of graphene sheets is prevented by incorporated Fe_3O_4 NPs/NSs, while graphene sheets serve as structural buffer and conductive network. Such synergistic effect between Fe_3O_4 and graphene maximize their electrochemical activity for energy storage applications in LIBs [43,44].

The rate capability of Fe_3O_4-NP/G and Fe_3O_4-NS/G composites were tested for 10 cycles at various current rates between 0.1 and 2 C (Fig. 5c). For Fe_3O_4-NS/G composites, the first discharge capacity is ~2090 mAh g^{-1} and capacity retention is ~1170 mAh g^{-1} after 10 cycles, whereas the reversible capacity of Fe_3O_4-NP/G composites rapidly drops from ~1880 to ~830 mAh g^{-1}. As the current rates are gradually increased

to 0.2, 0.5, 1.0, and 2.0 C, the corresponding reversible capacities of Fe_3O_4-NP/G and Fe_3O_4-NS/G composites are ~560 and ~1040 mAh g^{-1} for the 20th cycle, ~370 and ~830 mAh g^{-1} for the 30th cycle, ~270 and ~640 mAh g^{-1} for the 40th cycle, ~185 and ~440 mAh g^{-1} for the 50th cycles, respectively. It should be emphasized that the reversible capacity of Fe_3O_4-NS/G composites swiftly recovered to ~980 mAh g^{-1} when the current rate was brought down to 0.2 C after 50 cycles. The enhanced cyclic stability and rate capability of Fe_3O_4-NS/G composites can be ascribed to the advantage of their structural features as discussed previously. Compared with the previously reported Fe_3O_4 and graphene composites LIBs anodes, the Fe_3O_4-NS/G composites reported here exhibited superior electrochemical performance with higher specific capacity, better cyclic stability and rate capability [24,41,45–49].

EIS was used to further illustrate the origin of the improved electrochemical performance of Fe_3O_4-NS/G composites. The Nyquist plots (Z' *vs.* $-Z''$) of Fe_3O_4-NP/G and Fe_3O_4-NS/G composites are shown in Fig. 5d. The high-frequency semicircle is attributed to a passivation layer (SEI) formed which creates a corresponding impedance at the interface of the electrolyte and active material [50]. The semicircle in medium frequency describes the charge transfer impedance (R_{ct}) through the electrode/electrolyte interface, which is considered a large proportion of the overall cell's kinetic impedance [51]. The inclined line in the low frequency region is known as Warburg impedance, which represents the Li^+ ions diffusion/transport in the electrolyte to electrode's surface [52]. The size of the semicircles of Fe_3O_4-NS/G composites is smaller than that of Fe_3O_4-NP/G composites, showing a lower R_{ct}. The larger slope of Fe_3O_4-NS/G composites further demonstrates the faster diffusion/transport behavior of Li^+ ions in the electrolyte to electrode. These results further proved the advantage of the self-assembled mesoporous Fe_3O_4-NS/G composites for LIBs anodes.

4. Conclusion

We developed a graphene/acid assisted facile one-pot hydrothermal method to synthesize different morphologies of Fe_3O_4 and graphene composites. The morphology and structure of Fe_3O_4 can be tuned by adjusting the initial molar ratio between iron acetylacetonate and citric acid. In particular, mesoporous Fe_3O_4 NSs (~100 nm) self-assembled by numerous Fe_3O_4 NPs (~15 nm) are readily obtained using 3 mmol citric acid in the precursor solution. The synthetic method presented in this work can be used as a model framework to prepare similar structural features in other metal oxide and graphene composites with potential for enhanced electrochemical performance. The Fe_3O_4-NS/G composites deliver a high reversible capacity of ~1070 mAh g^{-1} after 160 cycles at a current density of 200 mA g^{-1}. It is believed that the self-assembled mesoporous Fe_3O_4-NS/G composites prepared in this work will have promising applications as high-performance anode materials for LIBs.

Acknowledgements

This work was fully supported by a Grant from the Innovation and Technology Funded Project (ITP/001/12NP) and the Research Grants Council of the Hong Kong, SAR China (CityU 122812).

Appendix A. Supplementary data

Supplementary data associated with this article can be found, in the online version, at http://dx.doi.org/10.1016/j.carbon.2015.01.062.

REFERENCES

[1] Armand M, Tarascon J-M. Building better batteries. Nature 2008;451:652–7.
[2] Liu C, Li F, Ma LP, Cheng HM. Advanced materials for energy storage. Adv Mater 2010;22:E28–62.
[3] Kaskhedikar NA, Maier J. Lithium storage ion carbon nanostructures. Adv Mater 2009;21:2664–80.
[4] Tarascon J-M, Armand M. Issues and challenges facing rechargeable lithium batteries. Nature 2001;414:359–67.
[5] Dunn B, Kamath H, Tarascon J-M. Electrical energy storage for the grid: a battery of choices. Science 2011;334:928–35.
[6] Poizot P, Laruelle S, Grugeon S, Dupont L, Tarascon J-M. Nano-sized transition-metal oxides as negative-electrode materials for lithium-ion batteries. Nature 2000;407:496–9.
[7] Li YG, Tan B, Wu YY. Mesoporous Co_3O_4 nanowire arrays for lithium ion batteries with high capacity and rate capability. Nano Lett 2008;8:265–70.
[8] Jeong JM, Choi BG, Lee SC, Lee KG, Chang SJ, Han YK, et al. Hierarchical hollow spheres of Fe_2O_3@polyaniline for lithium ion battery anodes. Adv Mater 2013;25:6250–5.
[9] Huang G, Zhang FF, Lei L, Du XC, Wang JW, Wang LM. Hierarchical $NiFe_2O_4/Fe_2O_3$ nanotubes derived from metal organic frameworks for superior lithium ion battery anodes. J Mater Chem A 2014;2:8048–53.
[10] Zhao NQ, Wu S, He CN, Wang ZY, Shi CS, Liu EZ, et al. One-pot synthesis of uniform Fe_3O_4 nanocrystals encapsulated in interconnected carbon nanospheres for superior lithium storage capability. Carbon 2013;57:130–8.
[11] Maier J. Nanoionics: ion transport and electrochemical storage in confined systems. Nat Mater 2005;4:805–15.
[12] Zhang WM, Wu XL, Hu JS, Guo YG, Wan LJ. Carbon coated Fe_3O_4 nanospindles as a superior anode material for lithium-ion batteries. Adv Funct Mater 2008;18:3941–6.
[13] Yue WB, Tao SS, Fu JM, Gao ZQ, Ren Y. Carbon-coated graphene–Cr_2O_3 composites with enhanced electrochemical performance for Li-ion batteries. Carbon 2013;65:97–104.
[14] Jung BY, Lim HS, Sun YK, Suh KD. Synthesis of Fe_3O_4/C composite microspheres for a high performance lithium-ion battery anode. J Power Sources 2013;244:177–82.
[15] Dong YC, Hu MJ, Ma RG, Cheng H, Yang SL, Li YY, et al. Evaporation-induced synthesis of carbon-supported Fe_3O_4 nanocomposites as anode material for lithium-ion batteries. CrystEngComm 2013;15:1324–31.
[16] Geim AK, Novoselov KS. The rise of graphene. Nat Mater 2007;6:183–91.
[17] Wu DQ, Zhang F, Liang HW, Feng XL. Nanocomposites and macroscopic materials: assembly of chemically modified graphene sheets. Chem Soc Rev 2012;41:6160–77.
[18] Novoselov KS, Geim AK, Morozov SV, Jiang D, Zhang Y, Dubonos SV, et al. Electric field effect in atomically thin carbon films. Science 2004;306:666–9.
[19] Chen H, Muller MB, Gilmore KJ, Wallace GG, Li D. Mechanically strong, electrically conductive, and biocompatible graphene paper. Adv Mater 2008;20:3557–61.

[20] Allen MJ, Tung VC, Kaner RB. Honeycomb carbon: a review of graphene. Chem Rev 2010;110:132–45.
[21] Yu GH, Hu LB, Liu N, Wang HL, Vosgueritchian M, Yang Y, et al. Enhancing the supercapacitor performance of graphene/MnO_2 nanostructured electrodes by conductive wrapping. Nano Lett 2011;11:4438–42.
[22] Liu F, Song SY, Xue DF, Zhang HJ. Folded structured graphene paper for high performance electrode materials. Adv Mater 2012;24:1089–94.
[23] Wei W, Yang SB, Zhou HX, Lieberwirth I, Feng XL, Müllen K. 3D graphene foams cross-linked with pre-encapsulated Fe_3O_4 nanospheres for enhanced lithium storage. Adv Mater 2013;25:2909–14.
[24] Liang CL, Zhai T, Wang W, Chen J, Zhao WX, Lu XH, et al. Fe_3O_4/reduced graphene oxide with enhanced electrochemical performance towards lithium storage. J Mater Chem A 2014;2:7214–20.
[25] Hummers WS, Offeman RE. Preparation of graphitic oxide. J Am Chem Soc 1958;80:1339.
[26] Ni ZH, Wang HM, Kasim J, Fan HM, Yu T, Wu YH, et al. Graphene thickness determination using reflection and contrast spectroscopy. Nano Lett 2007;7:2758–63.
[27] Zhou JS, Song HH, Chen XH, Zhi LJ, Yang SB, Huo JP, et al. Carbon-encapsulated metal oxide hollow nanoparticles and metal oxide hollow nanoparticles: a general synthesis strategy and its application to lithium-ion batteries. Chem Mater 2009;21:2935–40.
[28] Chen Y, Xia H, Lu L, Xue JM. Synthesis of porous hollow Fe_3O_4 beads and their applications in lithium ion batteries. J Mater Chem 2012;22:5006–12.
[29] Lee SH, Yu SH, Lee JE, Jin A, Lee DJ, Lee N, et al. Self-assembled Fe_3O_4 nanoparticle clusters as high-performance anodes for lithium ion batteries via geometric confinement. Nano Lett 2013;13:4249–56.
[30] Zhu T, Chen JS, Lou XW. Glucose-assisted one-pot synthesis of FeOOH nanorods and their transformation to Fe_3O_4@carbon nanorods for application in lithium ion batteries. J Phys Chem C 2011;115:9814–20.
[31] Chen JS, Tan YL, Li CM, Cheah YL, Luan D, Madhavi S, et al. Constructing hierarchical spheres from large ultrathin anatase TiO_2 nanosheets with nearly 100% exposed (001) facets for fast reversible lithium storage. J Am Chem Soc 2010;132:6124–30.
[32] Piao YZ, Kim HS, Sung YE, Hyeon T. Facile scalable synthesis of magnetite nanocrystals embedded in carbon matrix as superior anode materials for lithium-ion batteries. Chem Commun 2010;46:118–20.
[33] Wang L, Yu Y, Chen PC, Zhang DW, Chen CH. Electrospinning synthesis of C/Fe_3O_4 composite nanofibers and their application for high performance lithium-ion batteries. J Power Sources 2008;183:717–23.
[34] Laruelle S, Grugeon S, Poizot P, Dolle M, Dupont L, Tarascon J-M. On the origin of the extra electrochemical capacity displayed by MO/Li cells at low potential. J Electrochem Soc 2002;149:A627–34.
[35] Wu ZS, Ren WC, Wen L, Gao LB, Zhao JP, Chen ZP, et al. Graphene anchored with Co_3O_4 nanoparticles as anode of lithium ion batteries with enhanced reversible capacity and cyclic performance. ACS Nano 2010;4:3187–94.
[36] Pan DY, Wang S, Zhao B, Wu MH, Zhang HJ, Wang Y, et al. Li storage properties of disordered graphene nanosheets. Chem Mater 2009;21:3136–42.
[37] Yao WL, Yang J, Wang JL, Nuli Y. Multilayered cobalt oxide platelets for negative electrode material of a lithium-ion battery. J Electrochem Soc 2008;155:A903–8.
[38] Liu H, Wang GX, Wang JZ, Wexler D. Magnetite/carbon core-shell nanorods as anode materials for lithium-ion batteries. Electrochem Commun 2008;10:1879–82.
[39] Zhang HX, Feng C, Zhai YC, Jiang KL, Li QQ, Fan SS. Cross-stacked carbon nanotube sheets uniformly loaded with SnO_2 nanoparticles: a novel binder-free and high-capacity anode material for lithium-ion batteries. Adv Mater 2009;21:2299–304.
[40] Ma RG, He LF, Lu ZG, Yang SL, Xi LJ, Chung JCY. Large-scale fabrication of hierarchical alpha-Fe_2O_3 assemblies as high performance anode materials for lithium-ion batteries. CrystEngComm 2012;14:7882–7.
[41] Wang JZ, Zhong C, Wexler D, Idris NH, Wang ZX, Chen LQ, et al. Graphene-encapsulated Fe_3O_4 nanoparticles with 3D laminated structure as superior anode in lithium ion batteries. Chem Eur J 2011;17:661–7.
[42] Chen SQ, Wang Y. Microwave-assisted synthesis of a Co_3O_4-graphene sheet-on-sheet nanocomposite as a superior anode material for Li-ion batteries. J Mater Chem 2010;20:9735.
[43] Wang GX, Shen XP, Yao J, Park J. Graphene nanosheets for enhanced lithium storage in lithium ion batteries. Carbon 2009;47:2049–53.
[44] Paek SM, Yoo EJ, Honma I. Enhanced cyclic performance and lithium storage capacity of SnO_2/graphene nanoporous electrodes with three-dimensionally delaminated flexible structure. Nano Lett 2009;9:72–5.
[45] Zhou GM, Wang DW, Li F, Zhang LL, Li N, Wu ZS, Wen L, Lu GQ, Cheng HM. Graphene-wrapped Fe_3O_4 anode material with improved reversible capacity and cyclic stability for lithium ion batteries. Chem Mater 2010;22:5306–13.
[46] Li BJ, Cao HQ, Shao J, Qu MZ, Warner JH. Superparamagnetic Fe_3O_4 nanocrystals@graphene composites for energy storage devices. J Mater Chem 2011;21:5069–75.
[47] Chen WF, Li SR, Chen CH, Yan LF. Self-assembly and embedding of nanoparticles by in situ reduced graphene for preparation of a 3D graphene/nanoparticle aerogel. Adv Mater 2011;23:5679–83.
[48] Chen DY, Ji G, Ma Y, Lee JY, Lu JM. Graphene-encapsulated hollow Fe_3O_4 nanoparticle aggregates as a high-performance anode material for lithium ion batteries. ACS Appl Interfaces 2011;3:3078–83.
[49] Hu AP, Chen XH, Tang YH, Tang QL, Yang L, Zhang SP. Self-assembly of Fe_3O_4 nanorods on graphene for lithium ion batteries with high rate capacity and cycle stability. Electrochem Commun 2013;28:139–42.
[50] Aurbach D. Review of selected electrode-solution interactions which determine the performance of Li and Li ion batteries. J Power Sources 2000;89:206–18.
[51] Needham SA, Wang GX, Konstantinov K, Tournayre Y, Lao Z, Liu HK. Electrochemical performance of Co_3O_4-C composite anode materials. Electrochem Solid-State Lett 2006;9:A315–9.
[52] Fabio AD, Giorgi A, Mastragostino M, Soavi F. Carbon-poly(3-methylthiophene) hybrid supercapacitor. J Electrochem Soc 2001;148:A845–50.